Theoretical Notes
Note 195

SLA-73-0615

ON THE RADIATION-PRODUCED ELECTROMAGNETIC RESPONSE OF A DIELECTRIC-FILLED CYLINDRICAL CAVITY: A COMPARISON OF THEORY AND EXPERIMENT

F. B. Brumley, D. C. Evans, and D. L. Mangan*
Radiation Effects Division, 2115
Sandia Laboratories, Albuquerque, N.M. 87115

Printed December 1973

ABSTRACT

The electromagnetic response of a dielectric-filled finite-length cylindrical cavity, exposed end-on at the Hermes II radiation facility, is experimentally and theoretically examined. Loop sensors were used to obtain azimuthal-magnetic-field-related signals, and a dipole grid sensor was employed to acquire axial-electric-field-related signals. Both the experimental concept and the theoretical modeling are discussed in detail. The favorable comparison achieved between the experimentally obtained signals and the theoretically predicted results lends credence to the theoretical model developed.

*D. L. Mangan now in Division 2414

ACKNOWLEDGMENTS

Dr. L. D. Posey, supervisor of the Hermes II facility, provided pertinent consultation for this project. The Hermes II operations staff, supervised by Mr. J. E. Harness, gave valuable assistance in obtaining the experimental data. Mrs. M. L. Hauer expertly and graciously recorded the passive dosimetry data. Mr. E. F. Hartman provided the SANDYL electron-photon transport calculations. Mrs. S. N. Derado, Mrs. V. DeWitt, and Miss Ricarda Gallegos capably typed the manuscript. To all these people, the authors express their sincere gratitude.

TABLE OF CONTENTS

LIST OF ILLUSTRATIONS

LIST OF ILLUSTRATIONS (cont'd)

LIST OF TABLES

ON THE RADIATION-PRODUCED ELECTROMAGNETIC RESPONSE OF A DIELECTRIC-FILLED CYLINDRICAL CAVITY: A COMPARISON OF THEORY AND EXPERIMENT

Introduction

The gamma rates associated with typical radiation environments can produce, within cavities, distributed electron currents which are a driving source for electromagnetic fields. The coupling of these fields into circuits containing semiconductor devices or similar sensitive electronic components is of concern since short-duration, high-amplitude current pulses can permanently alter the device characteristics.[1] The electromagnetic response of a cavity driven by a radiation pulse must be understood for the effective design and assessment of the reliability of electronic packages and components which must perform within or after exposure to intense radiation fields.

The electromagnetic response of cylindrical cavities—evacuated, gas-filled, or dielectric-filled—have been examined theoretically by several authors.[2-7] Experimentally, the electromagnetic response of a large gas-filled cylindrical cavity exposed at the Hermes II facility has been investigated by Osborn.[8]

In this report, the authors examine, both experimentally and theoretically, the response of a small dielectric-filled cavity, the diameter of which is comparable to the radiation beam diameter at the anode of the Hermes II machine. The motivation for this study was the desire to assess, by experimentation, our capabilities in theoretically predicting the electromagnetic response of a cavity. Our experimental investigation was dual in nature. First, passive dosimetry was used to determine the spatial variation of the magnitude of the radiation within the cavity. This was done to quantify, for input into the theoretical investigation, the spatial variation of the axial and radial components of the radiation-produced driving current density. Second, various low-inductance loop sensors and a dipole grid sensor were used to measure implicitly the magnitude and temporal behavior of the magnetic and electric fields within the cavity. Concurrent with these measurements the authors obtained Compton diode signals and external passive dosimetry readings on each Hermes operation in order to establish, for the theoretical study, the temporal behavior and peak magnitude of the radiation-produced driving current density. The theoretical investigation involved the determination of the electric and magnetic fields within the cavity, as well as the subsequent coupling of these fields into equivalent circuits representing the low-inductance loops and the dipole grid sensor. In the remainder of this report are discussed the experimental investigations, the theoretical examination, and the comparison of the experimentally observed and theoretically predicted loop and dipole sensor signals.

Experimental Merchandise

The experimental investigation involved exposing a cylindrical electromagnetic cavity, end-on, to the radiation pulse of the Hermes II flash X-ray facility. All the experiments were performed by using identical cavity geometries. One cavity was used for dose mapping within the cavity. One cavity, which contained four different loop sensors, was used to obtain magnetic-field coupled signals. A third cavity, which contained a dipole grid sensor, was used to obtain axial-electric-field-induced signals.

Cavity Construction

The cavity geometry is shown in Figure 1. The two interchangeable end plates, or covers, and the separating central cylinder are made of 1.27-cm-thick aluminum. Four separate access ports, located 90 degrees apart and midway along the cylinder wall, allow electrical access to the cavity interior. These ports will accommodate either UG-422/U twinax and/or Gremar tri-axial electrical connectors. The pertinent dimensions of the cavity are also given in Figure 1.

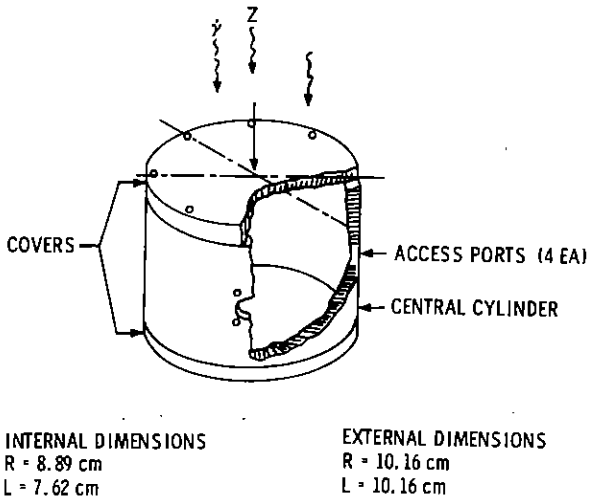

Figure 1. Experimental Cavity Geometry

Dielectric Medium

The dielectric medium used was commercially available Univolt 33 (Exxon) transformer oil. Pertinent data for this oil are listed in Table I.

TABLE I

Exxon Univolt 33 Transformer Oil Data

Specific Gravity	0.885-0.890
Dielectric Strength	118 kV/cm
Dielectric Constant	2.10-2.25
Constituents	
Hydrogen	13.0 wt%
Carbon	86.9 wt%
Sulfur	0.1 wt%
Water	<25 ppm
Compton Current Conversion Factor* for Hermes Spectrum	2.2×10^{-8} A/m^2 per rad ($AgPO_3$)†/sec

*Determined from photon-electron transport calculations by using SANDYL.

†Although the designation ($AgPO_3$) may be questionable (see, for example, Reference 9), its use is convenient for this report.

Dosimetry

The temporal behavior of the gamma pulse was equated to the signal obtained from a 6.4-cm-diameter Compton diode mounted on the cavity centerline, 1.8 cm behind the cavity rear face. Absolute dose was determined by using TLD-400 manganese-activated calcium fluoride dosimeters and/or silver-activated phosphate ($AgPO_3$) glass dosimeters. In obtaining the spatial distribution of the dose within the cavity, $AgPO_3$ glass dosimeters were used solely since the glass did not require a protective covering and could be placed directly in the oil medium. External absolute dosimetry (external to the cavity interior) involved both TLD-400 and $AgPO_3$ glass. A conversion factor[10] for rads(TLD-400)/rad($AgPO_3$) of 0.896 was used in the analysis.

Sensors

In order to measure the magnetic and electric fields implicitly within the cavity, two basically different types of sensors were required: (1) a low-inductance loop to obtain a magnetic-field-related signal and (2) a dipole grid sensor to record an axial-electric-field-related signal.

Loop sensor -- The signal obtained from a loop sensor is related to the time derivative of the magnetic field. Four different low-inductance loop sensors were used in the experiment. These were (1) a split-shield loop sensor, (2) a distributed split-shield loop sensor, (3) a moebius loop sensor, and (4) a distributed moebius loop sensor. The physical designs and electrical responses of these four types of loop sensors have been adequately discussed by Baum.[11,12] Briefly, both the split-shield and the moebius loop sensors are made of two pieces of coaxial cable. The two inner conductors at the output end of the loop are connected through a cavity access port to the two inner conductors of a RG-22B/U twinax cable. The ground sheaths of the two coaxial cables are connected to the ground sheath of the twinax. For a split-shield loop design, the inner

conductors at the other ends of the coaxial cables are connected and the sheaths are left open. For a moebius loop sensor design, the inner conductor of one of the coaxial cables is connected to the outer sheath of the other coaxial cable and vice versa. The strip loop is, in effect, a single-turn pickup loop of slightly lower inductance, and the moebius loop is a two-turn pickup loop of slightly larger inductance. The adjective "distributed" applied to either of these two loop designs implies that the loop has been wrapped around a cylindrical conducting tubing, or core, which lowers the inductance of the loop. The moebius loop design has an advantage over the split-shield design because the effects of Compton electron currents driven from the outer sheath to the inner conductor are minimized. The moebius loop, because of its two-turn design, also yields a higher signal than the split-shield loop. The main disadvantage of the moebius loop design, when compared to the split-shield design, is that it necessarily has a higher inductance and thus a lower frequency response. In the experimental setup employed here, all loop sensors were connected to 95-ohm RG-22B/U twinax transmission line. Pertinent data associated with the loop sensors are presented in Table II. The inductance values were obtained by using a Hewlett-Packard 4815A vector impedance meter. All the loops were constructed from RG-223/U coaxial cable. For the distributed loop designs, the inner conductor core was made by wrapping 0.01-cm-thick, 5.1-cm-wide copper foil around a polyethylene rod of appropriate diameter and comparable length. The locations of the four loops, within the cavity, are depicted in Figure 2.

TABLE II

Loop Sensor Data

Sensor Type	Radius (cm)	Inductance (μh)
Split-Shield Loop (L1)	2.82	0.200
Distributed Split-Shield Loop (L2)	1.06	0.095
Moebius Loop (L3)	2.78	0.500
Distributed Moebius Loop (L4)	1.06	0.125

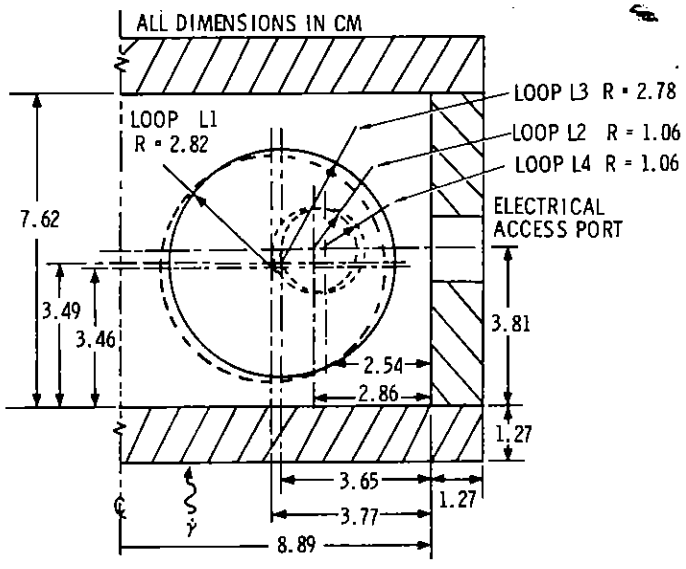

Figure 2. Locations of the Loop Sensors Within the Cavity

Dipole Grid Sensor -- The parallel-plate dipole grid sensor, used to measure axial-electric-field-related signals, in actuality has as its driving function the potential voltages on the plates of the dipole. The designs of dipole grid sensors for use in measuring IEMP-related electric fields have been previously reported.[13,14] The only dipole sensor design considered for this experiment was constructed of two 1.9-cm-radius copper-wire-fabric discs separated by a 0.825-cm-thick polyethylene disc. The wire fabric was made of interwoven 0.028-cm copper wire and had a spacing of 7.1 by 5.5 wires per cm. Wire mesh is used, as opposed to a solid metal plate, to reduce Compton interactions. The two grids were connected to the two inner conductors of a twinax transmission line. Pertinent data for the grid sensor are noted in Figure 3, which depicts the location of the sensor within the cavity. The relevant capacities noted in this figure were measured with the vector impedance meter.

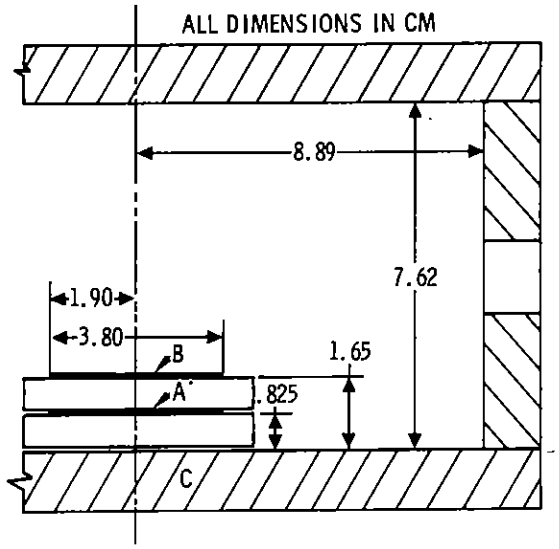

C_{AB} = (2.6pf + DISTRIBUTED LEAD CAPACITANCE) = 10.9pf
C_{AC} = 6.9pf
C_{BC} = 3.6pf

Figure 3. Location of the Dipole Grid Sensor Within the Cavity

Recording Instrumentation

The average Hermes II pulse has a full width at half maximum of 50 to 55 nsec. The base width of the pulse is ~150 nsec. The frequency spectrum shown in Figure 4 can be obtained through use of a $\cos^2 t$ curve to represent a generic Hermes II pulse. The 3-db point is near 5.4 MHz. Experimentally, however, each Hermes II pulse has its own individual shape, and small-amplitude components with frequencies exceeding 125 MHz superimposed on the basic waveform are common. For the cavity size used in this investigation, the lowest resonant frequency,[3] with zero conductivity assumed, is 1.2 GHz. In some respects, therefore, our experimental investigation is limited by the frequency response of the oscilloscopes used (see Table III).

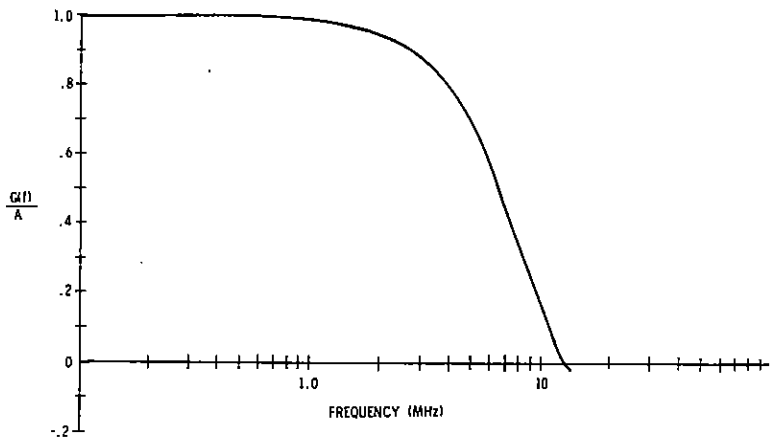

Figure 4. Frequency Spectrum for Cos^2t Generic Hermes II Pulse

TABLE III

Oscilloscope Data

Tektronix Model	Bandwidth (MHz)	Risetime (nsec)
454	150	2.4
454A	150	2.4
485	350	1.0
7904 (7A19 Vertical Plug-in)	500	0.8

All the oscilloscopes were triggered in parallel by means of a Bishop five-port splitter coupled to a TRW pulse generator. A separate Compton diode was employed to trigger the TRW instrument.

Transmission Lines

Cable lengths of not less than 15 meters are required to transmit signals from the Hermes II experimental area, where the cavity was located, to the South Screen Room, where the recording instrumentation was located. Therefore, 15 meters of RG-213/U coaxial line was used to carry the Compton diode signal which triggered the TRW pulse generator.

Three other signal lines were used for actual data transmission. The signal from the Compton diode located directly behind the cavity was transmitted on 23 meters of RG-213/U coaxial cable. The sensor signals originating within the cavity were transmitted on 23 meters of RG-22B/U twinax cable wrapped with conductive zipper tubing.

At the present time, only 50-ohm coaxial feedthrough connectors are provided for feeding signals into the South Screen Room and, unless these connectors are used, the shielding characteristics of the screen room may be compromised. Therefore, external to the screen room and located in a Faraday cage, a North Hills Electronics 0200FA Ballun was used to transform the

twinax 95-ohm line to 50-ohm coaxial line. Triaxial RG-223/U was used to transmit the transformed signal from the output of the Ballun to the screen room feedthrough. An entire sensor-signal-to-transmission system, excluding the RG-213/U coaxial cable hookup inside the screen room connecting the feedthrough to a scope, is shown in Figure 5.

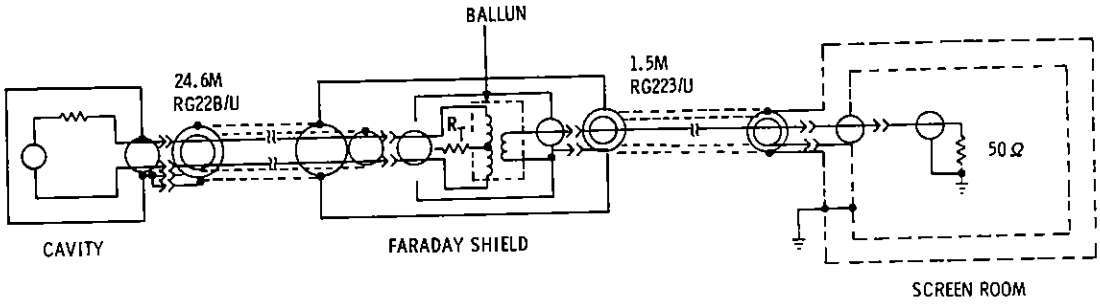

Figure 5. Electrical Transmission System

It should be noted that an appropriately determined resistor placed between the Ballun center tap and the twinax shield (denoted by R_T in Figure 5) will properly terminate common-mode signals present on the twinax lines. The value of the resistor was determined by using time domain reflectometry (TDR) techniques. Applying a common-mode rectangular pulse of 25-nsec duration and 145-volt amplitude at the cavity end of the signal transmission system, common-mode rejection ratios of greater than 16 were determined from the signals obtained at the scope end of the system. As an additional verification that sufficient common-mode rejection was being achieved, the signal generated in a Hermes II environment with a short placed across the cavity twinax feedthrough was recorded and found to be in the neighborhood of 1 volt, peak to peak (VPP). Normal sensor signals were greater than 10 VPP.

Thoughts on Theory

The theoretical investigation involved, first, determining the electromagnetic response of the cylindrical cavity exposed end-on to the Hermes II radiation pulse. The resultant electric and magnetic fields were then used as source functions for the respective sensor equivalent circuits, and the outputs from these circuits were calculated. In this section the theoretical model used to predict the electromagnetic response of the cavity and the equivalent circuits used to predict the oscilloscope traces are discussed.

Theoretical Model

The theoretical model considered for this investigation has, in part, been reported previously in the literature.[3, 4, 7] The geometry is shown in Figure 6. Azimuthal symmetry is assumed. By imposing the boundary condition that the tangential components of the electric fields vanish at the inner walls of the conducting surfaces, it can be readily shown[3] that the nonzero components of the electromagnetic response are the axial electric field (E_Z), the radial electric

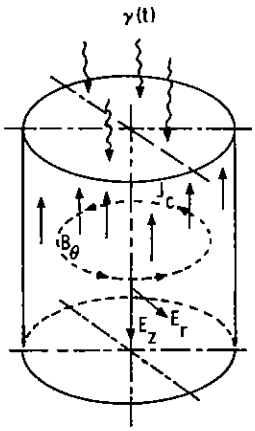

Figure 6. Theoretical Model Geometry

field (E_r), and the azimuthal magnetic field (B_θ). For IEMP-type problems, it is convenient to write Ampere's Law as

$$\nabla \times (\vec{B}/u) = \vec{J}_c + \sigma\vec{E} + \frac{\partial(\epsilon\vec{E})}{\partial t}, \tag{1}$$

where the radiation-produced Compton current ($\vec{J}_c$) has been separated from the conduction current ($\sigma\vec{E}$) and the displacement current ($\partial(\epsilon\vec{E})/\partial t$). Faraday's Law is written in its usual form:

$$\nabla \times \vec{E} = -\frac{\partial\vec{B}}{\partial t} . \tag{2}$$

With $\vec{J}_c$, the conductivity of the cavity medium (σ), the medium permittivity (ϵ), and the medium permeability (μ) completely specified, $\vec{E}$ and $\vec{B}$ can be determined from the above two equations by using finite difference techniques. Such a computer code, developed by one of the authors (Mangan) and labeled NUCYL,* uses a staggered leap frog scheme to increment the field components in time. An interwoven spatial mesh is used to facilitate the calculations of the curl operators and to implement the boundary conditions outlined above. The code allows for the medium properties (σ, ϵ and μ), as well as $\vec{J}_c$, to be arbitrary functions of space and time, provided that the assumption of axial symmetry is not violated.

Compton Current Density

The temporal behavior of $\vec{J}_c$ was assumed to be identical to that of the Compton diode signal. The spatial variation in the magnitude of $\vec{J}_c$ was assumed to be the same as the spatial variation of the dose deposition within the cavity medium. The direction of the current density was assumed to follow the normals to the isodose curves within the cavity. Specifically, by making allowances for the pulse to travel across the medium with the speed of light,

$$\vec{J}_c(r, z, t - z/c) = K\dot{\gamma}_{max} f(t - z/c)\, g(r, z)\nabla g(r, z)/|\nabla g(r, z)| . \tag{3}$$

*The computer code NUCYL has not yet been formally reported. Sufficient details of the code, however, have been discussed in Reference 4.

Here, K is the Compton current conversion factor (see Table I), $\dot{\gamma}_{max}$ is the peak dose rate (rads/sec) at the front inside face of the cavity, f(t) is the time-dependent Compton diode signal normalized to unity, and g(r, z) specifies the spatial distribution of the dose within the cavity medium normalized to the dose at the front inside face of the cavity.

Loop Sensor Equivalent Circuit

The equivalent circuit[11] used for the loop sensors is presented in Figure 7. The inductance value for each of the types of loop sensors has been specified in Table II. Z_o represents the differential impedance of the RG-22B/U twinax cable.

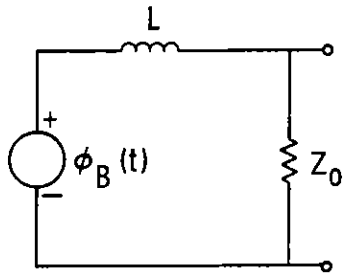

Z_0 (95Ω DIFFERENTIAL IMPEDANCE RG -22B / U)
L (LOOP INDUCTANCE)

Figure 7. Loop Sensor Equivalent Circuit

The magnetic-field-related driving potential $\phi_B(t)$ is calculated from an integration of Equation 2 over a sensor loop area.

$$\int(\nabla \times \vec{E}) \cdot d\vec{A} = -\int(\partial\vec{B}/\partial t) \cdot d\vec{A} \qquad (4)$$

or, equivalently,

$$\phi_B(t) \equiv \oint \vec{E} \cdot d\ell = -\int \dot{B}_\theta dA \,. \qquad (5)$$

The computer code NUCYL computes and stores the time derivative of magnetic field $\dot{B}_\theta(t_k, i, j)$ at time t_k and at the space node point (i, j) within the cavity. Since uniform space meshing is employed in the computer code, the elemental area ($\Delta A = \Delta r \Delta z$) associated with any mesh point (i, j) is constant. $\phi_B(t_k)$ is readily calculated by summing $\dot{B}_\theta(t_k, i, j)$ over all i and j values that lie within or on the boundary defined by the sensor loop. In Figure 8, the area summed to determine $\phi_B(t_k)$ for loop L3 (see Table II) is compared to the actual area of loop L3.

A digital computer code was written to simulate the response across the resistor in the loop sensor equivalent circuit for a specified digitized driving function ($\phi_B(t_k)$). This response is compared to the experimentally obtained loop sensor signal.

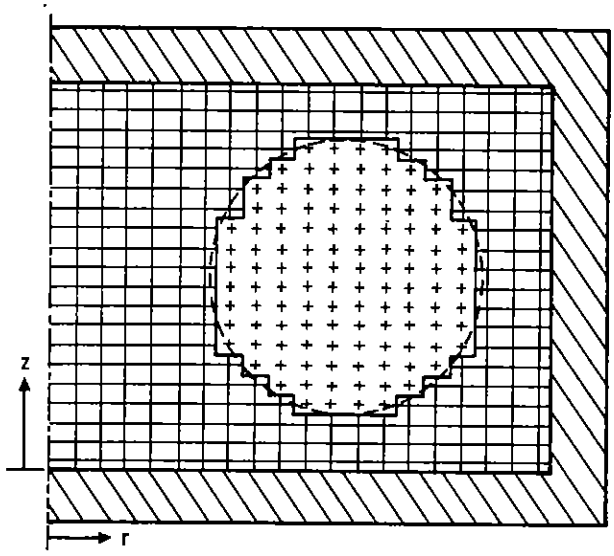

Figure 8. Comparison of Loop Sensor Area and Finite Difference Area

Dipole Grid Sensor Equivalent Circuit

The equivalent circuit used to represent the dipole grid sensor is shown in Figure 9. The potential function $\phi_1(t)$ represents the potential (with respect to the cylinder wall) that the grid closest to the Hermes II anode would reach if no conduction or capacity coupling existed between the grid and the cylinder wall or between the grids of the dipole and if the grid was not connected to any external circuitry. Specifically, it is the potential calculated from the electromagnetic response determined by the NUCYL code. The designation $\phi_2(t)$ represents the corresponding potential of the grid farthest from the Hermes II anode. The two $0.5Z_o$ resistors represent the common-mode impedance of the RG-22B/U twinax. R_1 and C_1 represent the resistance and the capacitance inside the cavity region between the cylinder wall and the grid located closest to the Hermes II anode. R_2 and C_2 are those between the wall and the other grid. R_3 and C_3 represent the resistance and the capacitance between the two grids. The capacitances are those specified in Figure 3, and the corresponding resistance values were proportioned as $RC = \epsilon/\sigma$ where ϵ and σ are the medium permittivity and conductivity. The inductance in the circuit represents the lead inductance.

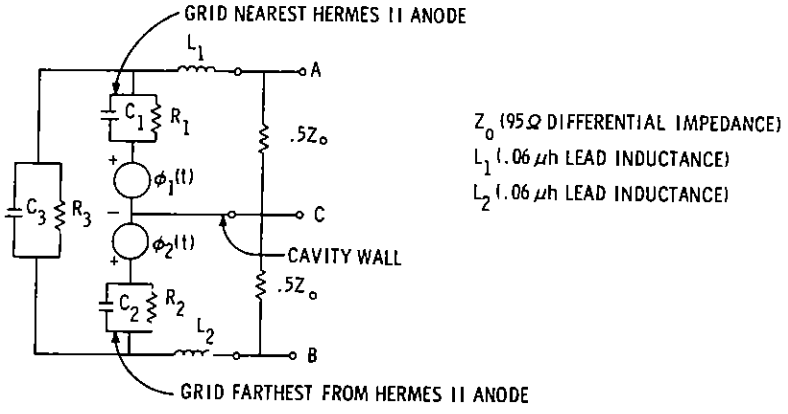

Figure 9. Dipole Grid Sensor Equivalent Circuit

With z_1 and z_2 representing the distances of the grid located nearest the Hermes II anode and the grid located farthest from the anode, respectively, the potentials $\phi_1(t)$ and $\phi_2(t)$ were obtained from the NUCYL code results by using finite difference equivalents of the following equations:

$$\phi_1(t_k) = \left(\int_o^{z_1} E_z(t_k, r, z)dz \right)_{ave} \tag{6}$$

and

$$\phi_2(t_k) = \left(\int_o^{z_1} E_z(t_k, r, z)dz \right)_{ave} . \tag{7}$$

Here, the average was performed over all radius node positions (r_i) so that $0 \leq r_i \leq r_g$ where r_g represents the grid sensor radius. A digital computer code was written to determine the differential response across the two $0.5Z_o$ resistors of the dipole grid sensor equivalent circuit when driven by the digitized time behavior of the two potential functions, $\phi_1(t_k)$ and $\phi_2(t_k)$. It is this response that is compared to the experimentally obtained signals. Although only one dipole grid sensor design was considered for the experiment, two experimental signals were obtained. One was with the grid sensor located toward the rear of the cavity and one was with the cavity turned around or, equivalently, with the grid sensor located toward the front of the cavity.

On Comparing Experiment and Theory

The theoretical predictions and experimental results are closely coupled because part of the experimentally determined results were required to adequately specify the spatial and temporal behavior of the Compton-produced current density ($\vec{J}_c$) which was needed to predict the electromagnetic response of the cavity. In this section is discussed the means by which the dose deposition profile within the cavity was obtained. This profile was the basis for specifying the spatial variation, as well as the direction of J_c. The measured electrical signals and the predicted signals for the four loop sensors when the cavity is exposed to the Hermes II radiation environment are then compared. Finally, the same comparison is made for the dipole grid sensor signals.

Dose Mapping

The motivation for determining the dose profile within the cavity medium was that the magnitude of the Compton current will scale proportionally to the dose.[15] Also, the net flux of electrons will be in the direction of the incident photon flux. For a spatially nonuniform electron flux possessing azimuthal symmetry, the current density will have two components, J_z and J_r. The relative magnitude of these components can be predicted by defining the normals to the isodose lines within the cavity.

To determine the spatial variation in the magnitude of the dose within the cavity, an array of 94 $AgPO_3$ dosimeters and 10 TLD-400 dosimeters was used inside and outside the cavity. The arrangement of the dosimeters within the cavity can best be described as a spiral staircase when viewed down the axis of the cavity. Six rows, each with 13 $AgPO_3$ dosimeters, were arranged in the staircase array, with the first row at a clock position of 12:00 and the remaining five rows at positions 1:00 through 5:00. The radial positions of the dosimeters along any row were nonsymmetrical with respect to the cavity centerline and alternating rows were reversed to insure that, during the Hermes II photon flux exposure, no dosimeter was shielded by another. In addition to the internal dosimetry, similar rows of $AgPO_3$ and TLD-400 dosimeters were arranged on the front face of the cavity at 2:30; the rear face, at 3:30. Since, as it is said, one picture is worth ten thousand words,[16] Figures 10 and 11 are presented to depict the array.

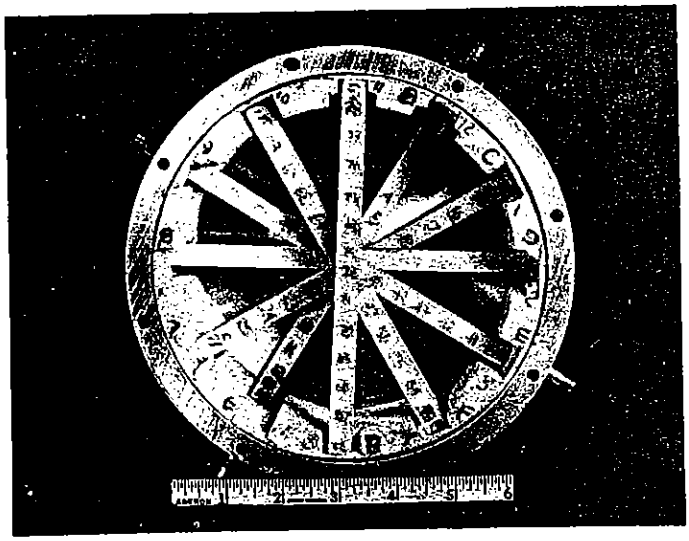

Figure 10. Photograph of the Dosimetry Array Used for Dose Mapping Within the Cavity

The raw data, normalized to 50,000 rads ($AgPO_3$), obtained from a single Hermes II operation (No. 8034), are presented in Table IV.

The data used for dose profile mapping were determined from the raw data by folding the latter about the centerline and, beginning with the outer radius position, averaging the sequential pairs of dose and their corresponding radial positions. These data are presented in Table V.

The data of Table V, plotted in Figure 12 as a function of radial position for the axial location held fixed, are the basis for the determination of the function g(r, z) used in Equation 3.

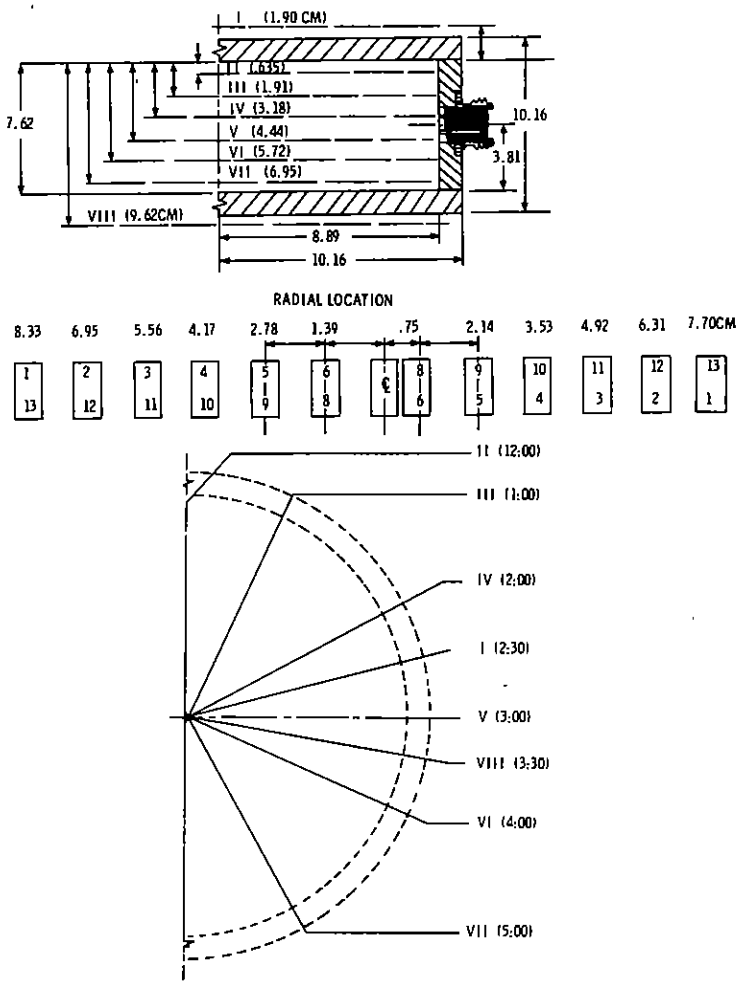

Figure 11. Dosimetry Array Used for Dose Mapping Within the Cavity

TABLE IV

Raw Data Obtained for Dose Profile Mapping, Normalized to 50,000 Rads ($AgPO_3$). (* Indicates a TLD-400.)

Z \ R	1	2	3	4	5	6	7	8	9	10	11	12	13
I	0.960*	1.100	1.200	1.249*	1.206	1.184	1.172*	1.184	1.244	1.221*	1.320	1.382	1.272
II	0.886	0.834	0.920	0.954	0.948	0.932	0.924	0.938	0.948	0.924	0.944	0.952	0.870
III	0.520	0.630	0.744	0.834	0.854	0.886	0.870	0.904	0.886	0.888	0.918	0.888	0.866
IV	0.520	0.572	0.662	0.774	0.778	0.796	0.808	0.814	0.814	0.846	0.838	0.824	0.740
V	0.416	0.496	0.604	0.686	0.692	0.728	0.750	0.756	0.772	0.756	0.744	0.698	0.624
VI	0.476	0.556	0.630	0.664	0.285	0.698	0.704	0.704	0.686	0.662	0.612	0.526	0.434
VII	0.392	0.480	0.556	0.608	0.640	0.644	0.644	0.644	0.630	0.602	0.560	0.518	0.436
VIII	0.237*	0.276	0.290	0.397*	0.454	0.458	0.513*	0.512	0.518	0.509*	0.442	0.406	0.384

TABLE V

Averaged Data Used for Dose Profile Mapping, Normalized to the Dose at the Inside Front Cover of the Cavity

Z \ R	1-13	2-12	3-11	4-10	5-9	6-8	℄
I	1.202	1.286	1.306	1.237	1.269	1.227	1.215
II	0.806	0.925	0.966	0.973	0.982	0.969	0.958
III	0.718	0.787	0.861	0.892	0.902	0.895	0.902
IV	0.653	0.723	0.777	0.824	0.825	0.834	0.831
V	0.539	0.619	0.698	0.747	0.748	0.769	0.777
VI	0.472	0.561	0.644	0.687	0.711	0.726	0.730
VII	0.429	0.517	0.578	0.578	0.627	0.658	0.667
VIII	0.321	0.353	0.379	0.469	0.504	0.503	0.521

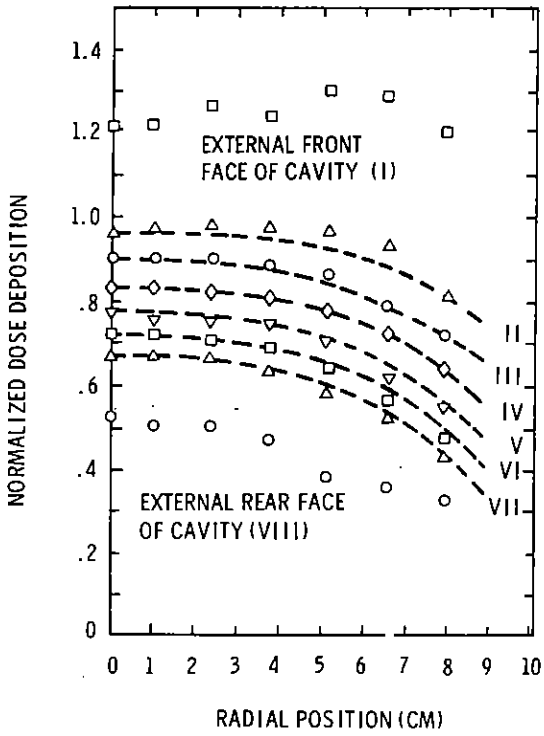

Figure 12. Radial Variation of the Dose Deposition Within and External to the Cavity, Normalized to the Maximum Dose at the Inside Front Cover of the Cavity

To facilitate inputting the NUCYL code to allow for the spatial variation of J_c, as well as the determination of $\nabla g(r, z)$, analytical expressions for $g(r, z)$ were determined for the data plotted in Figure 12. These expressions are

$$g(r, z) = \exp(-0.058z) \qquad 0 \leq r \leq 1.07 \text{ cm} \tag{8a}$$

and

$$g(r, z) = 1.08\left[\exp(-0.058z) - 0.858\exp(-0.099z)\right]\{1 - \exp(0.375r - 3)\} + 0.858\exp(-0.099z) \qquad 1.07 \text{ cm} \leq r \leq 8.89 \text{ cm} \tag{8b}$$

where r and z are in cm. The analytical values for $g(r, z)$ are plotted as dashed lines in Figure 12. In Figure 13 the data and the function $g(r, z)$ are plotted as a function of z for two r positions held fixed. The corresponding isodose curves within the cavity, normalized to the dose at the inside face of the front cover, are plotted in Figure 14.

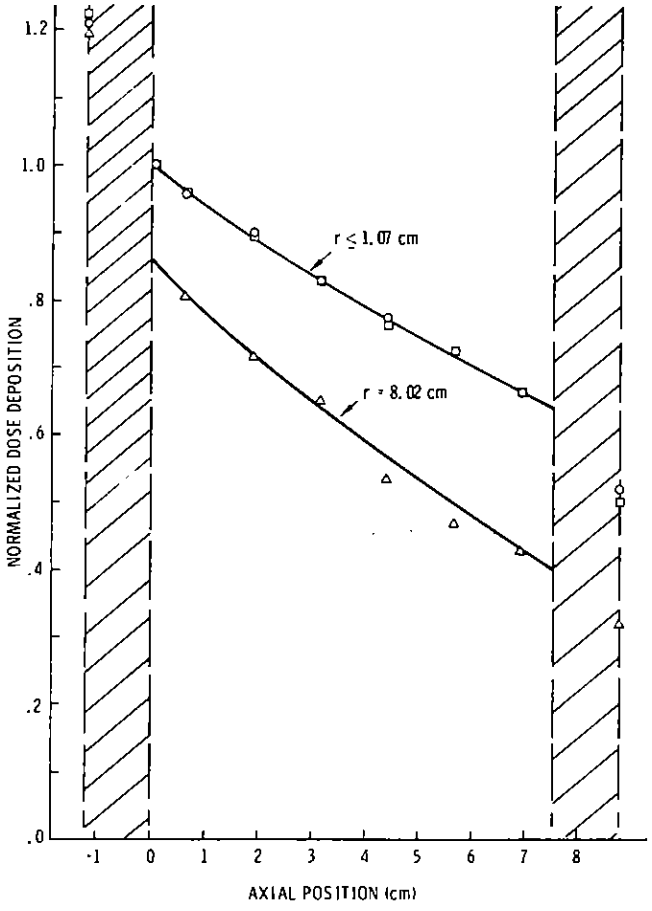

Figure 13. Axial Variation of the Dose Deposition Within and External to the Cavity, Normalized to the Maximum Dose at the Inside Front Cover of the Cavity

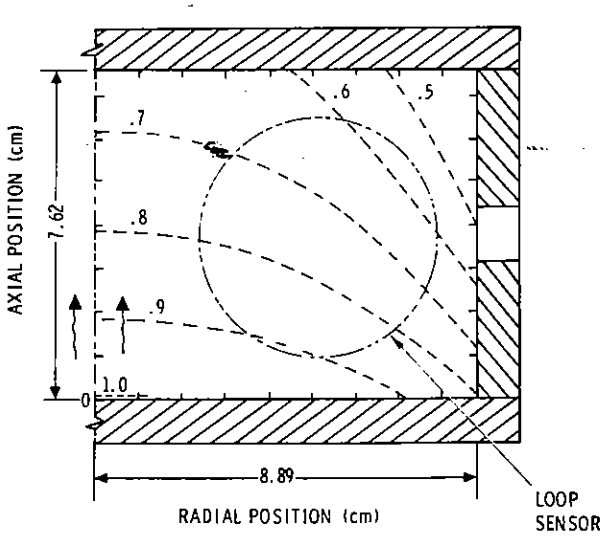

Figure 14. Isodose Profile Within the Cavity, Normalized to the Maximum Dose at the Inside Front Cover of the Cavity

Compton Diode Signals

Required for the theoretical calculations were the normalized (to unity) temporal behavior of the Compton current density, denoted f(t) in Equation 3, and the peak gamma dose rate, $\dot{\gamma}_{max}$. The temporal behavior of the current density pulse was equated to the temporal behavior of the Compton diode signal. The peak dose rate for a particular Hermes II operation was determined by relating the time integral of the Compton diode signal to the corresponding total dose obtained with TLD-400 dosimeters mounted, external to the cavity, in the positions denoted by an asterisk in Table IV. All Compton diode signals were recorded with the Tektronix 485 scope. In Figure 15, the Compton diode is shown mounted to the back face of the cavity.

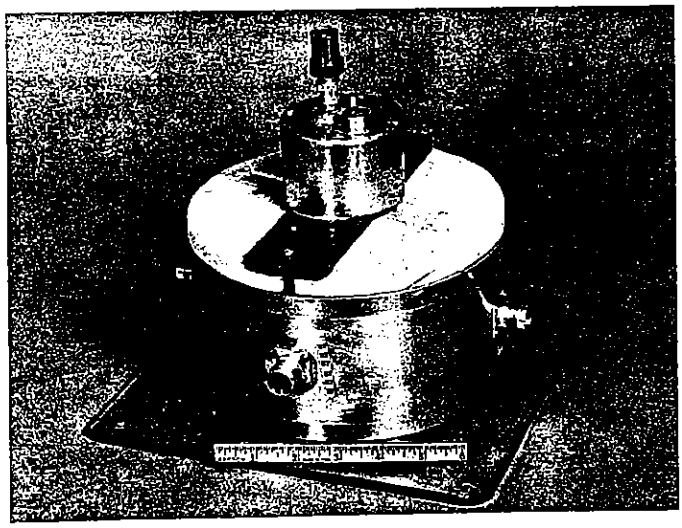

Figure 15. Photograph of the Compton Diode Mounted on the Rear of the Cavity

Theoretical Calculations

The temporal signature and spatial distribution of the output of each Hermes II operation varies from shot to shot. In the theoretical predictions presented below, the spatial distribution of the dose deposition within the cavity for each Hermes II operation was assumed to be that given by Equations 8a and 8b. The temporal behavior of the Compton current density, however, was individually considered in the theoretical analysis of each Hermes II operation. Specifically, the theoretical prediction associated with a particular sensor signal was calculated by use of the Compton diode temporal behavior recorded during the same Hermes II operation in which the sensor signal was obtained.

In the theoretical calculations, the electrical properties ϵ, μ and σ were assumed to be constant. The permittivity (ϵ) was specified as 1.9×10^{-11} farads/m. The permeability (μ) was set equal to $4\pi \times 10^{-7}$ henrys/m. It was realized that the photoconductivity of the dielectric medium is time dependent;[17,18] however, the conductivity was assumed to be constant and equal to 8×10^{-4} mhos/m, which is approximately the peak photoconductivity of polyethylene to be expected at the peak dose rates experienced with the Hermes II environment. The photoconductivity was necessarily specified as a constant because the authors did not feel that adequate data defining the temporal behavior were available. Also, the value associated with polyethylene was used throughout the cavity, since a value for oil has not, to our knowledge, been determined. In determining the various resistance values needed for the dipole grid equivalent circuit, the value of σ used was also 8×10^{-4} mhos/m.

Loop Sensor Signals

Figure 16 shows the location of the four loop sensors mounted in the cavity. The instrumentation capability allowed recording of two loop sensor signals during a single Hermes II operation. The "noise" which can be associated with all the experimental observations is 1 VPP. A typical noise pulse, shown in Figure 17, was obtained with a short, instead of a sensor, placed across the feedthrough terminals of the cavity.

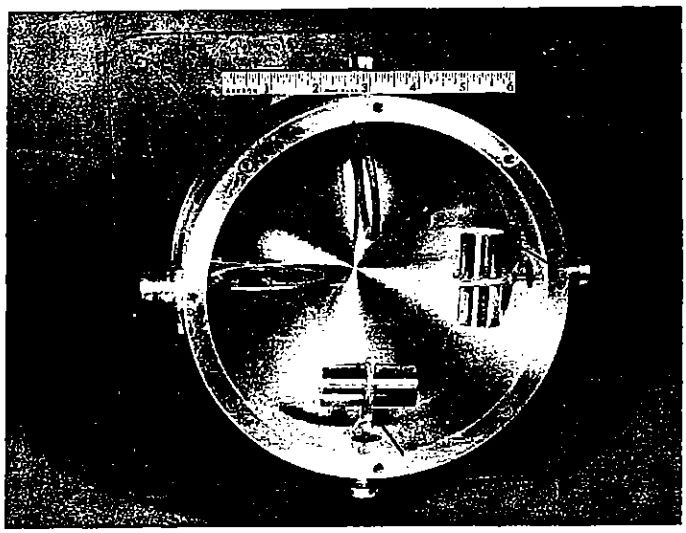

Figure 16. Photograph of the Loop Sensors Mounted Within the Cavity

On the graphs comparing experiment and theory, the data were plotted so that the pulses cross from positive to negative simultaneously.

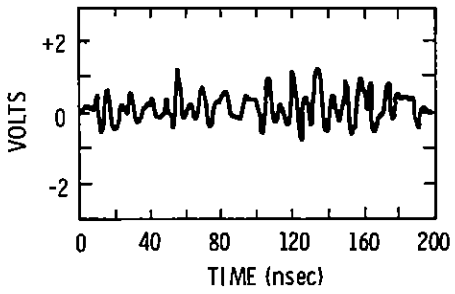

Figure 17. Typical Noise Signal

Split-Shield Loop Sensor (L1) Signal -- The split-shield loop sensor signal was obtained in the Hermes II operation No. 8036 radiation environment. The Compton diode signal associated with this operation is presented in Figure 18. The loop sensor signal was recorded on the Tektronix 454A scope. The experimental observation and theoretical prediction are compared in Figure 19.

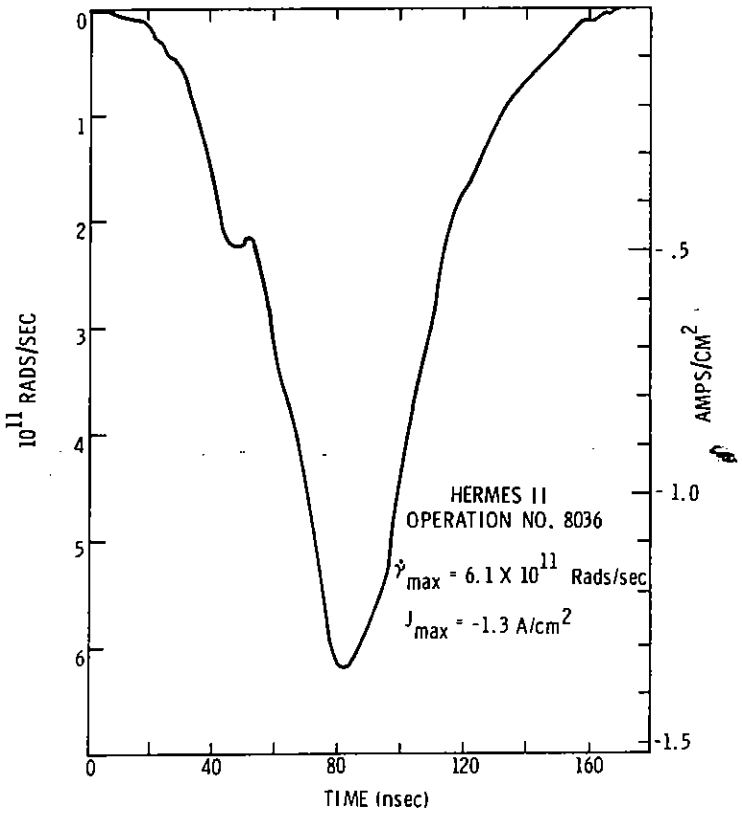

Figure 18. Compton Diode Signal for Hermes II Operation No. 8036

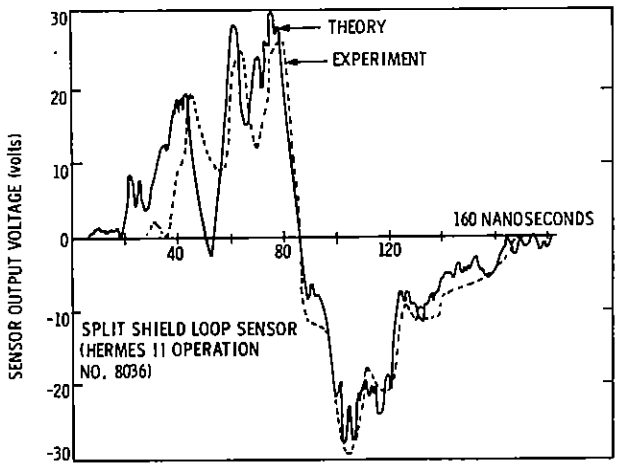

Figure 19. Comparison of Experimental Observation and Theoretical Prediction for the Split-Shield Loop Sensor

Distributed Split-Shield Loop Sensor (L2) Signal -- The signal from the distributed split-shield loop sensor was obtained on Hermes II operation No. 8037. The relevant Compton diode signal is shown in Figure 20. The experimental observation, recorded with the Tektronix 7904 scope, and the theoretical prediction are compared in Figure 21. The magnitude of the L2 loop sensor signal is smaller than that of the L1 because the area of the former loop is smaller than that of the latter (see Figure 2). Also, the frequency content of L2 is higher, because it has a lower inductance (see Table II).

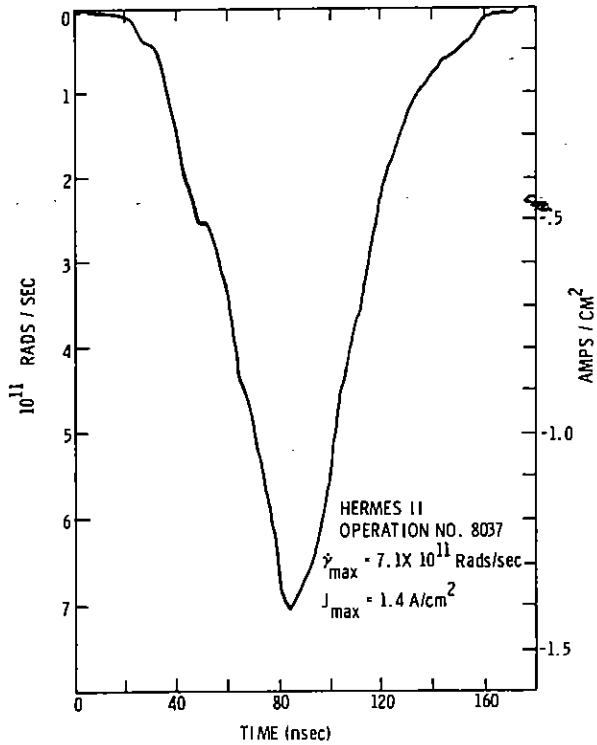

Figure 20. Compton Diode Signal for Hermes II Operation No. 8037

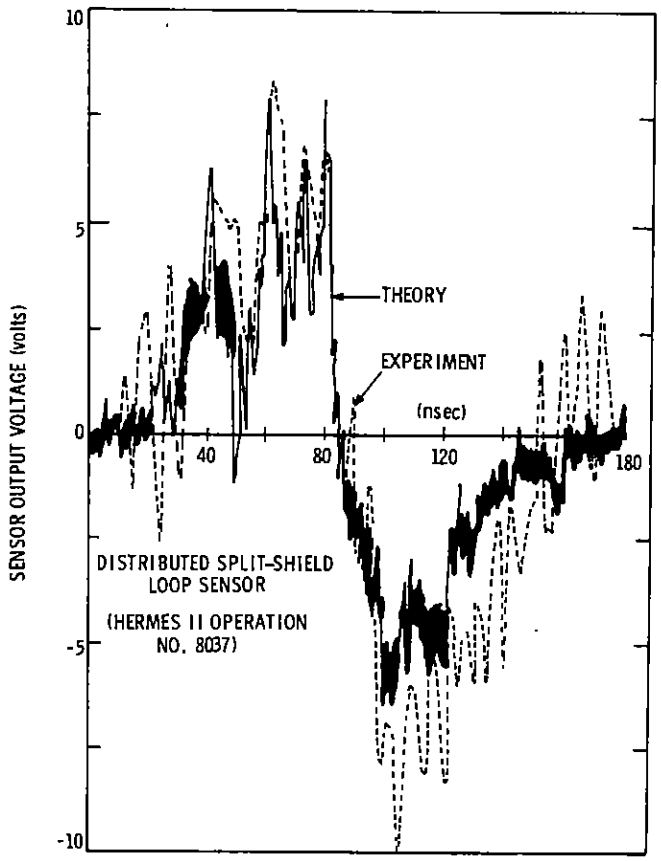

Figure 21. Comparison of Experimental Observation and Theoretical Prediction for the Distributed Split-Shield Loop Sensor

Moebius Loop Sensor (L3) Signal -- The signal from L3 was obtained on Hermes II operation No. 8036 (Figure 18). The experimental signal was recorded on the Tektronix 7904 scope. Experiment and theory are compared in Figure 22. With the L1 signal used as reference, the magnitude of the L3 signal is higher because L3 is, in effect, a two-turn loop sensor and L1 is a single-loop sensor. Because of inductances, the L3 signal has a lower frequency content than L1.

Distributed Moebius Loop Sensor (L4) Signal -- The signal from this loop was obtained in the Hermes II operation No. 8037 radiation environment (Figure 20). The experimental observation, recorded on the Tektronix 454A scope, and the theoretical prediction are presented in Figure 23. Again, the differences in loop area and inductance are reasons for the differences in magnitude and frequency content when the L3 and L4 signals are compared.

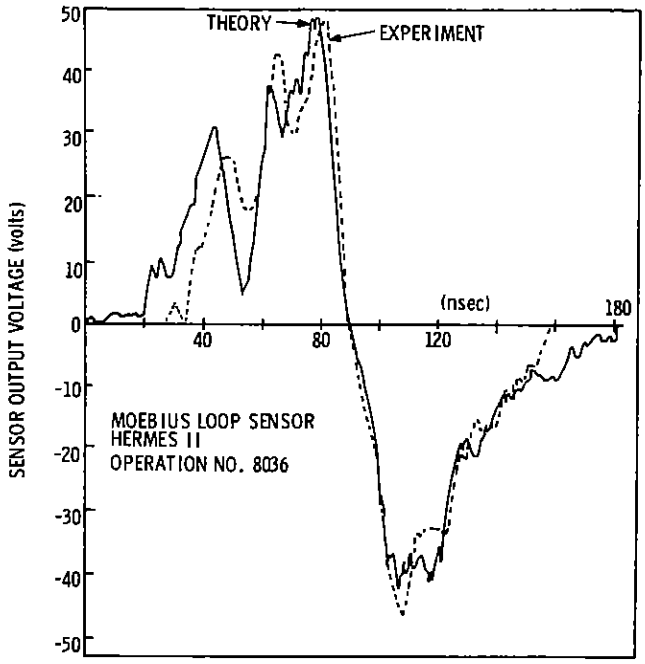

Figure 22. Comparison of Experimental Observation and Theoretical Prediction for the Moebius Loop Sensor

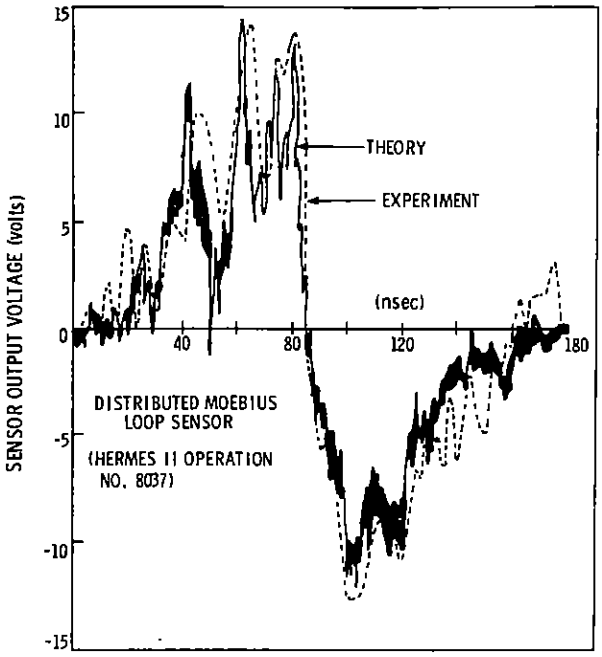

Figure 23. Comparison of Experimental Observation and Theoretical Prediction for the Distributed Moebius Loop Sensor

Dipole Grid Sensor Signals

Two experimental signals were obtained with the dipole grid sensor. One was with the sensor located toward the rear of the cavity (radiation incident from the top of Figure 3), and the other was with the cavity turned around (radiation incident from the bottom of Figure 3). A photograph showing the dipole grid sensor mounted in the cavity is presented as Figure 24. Again, the noise associated with the experimental observations is ~1 VPP. On the plots comparing theory and experiment, the data were plotted so that the peaks of the two curves occurred simultaneously.

Rear Location -- The axial-electric-field-related signal with the dipole grid sensor located in the rear of the cavity was obtained in the Hermes II operation No. 8033 radiation environment. The Compton diode signal for this operation is shown in Figure 25. The experimental observation, recorded on the Tektronix 7904 scope, and the theoretical prediction are compared in Figure 26.

Front Location -- The signal obtained with the dipole grid sensor mounted in the front of the cavity was obtained in the Hermes II operation No. 8028 environment. The Compton diode trace is presented in Figure 27. Experiment and theory are compared in Figure 28. The Tektronix 7904 scope was used to record the experimental observation.

The polarity of the dipole grid sensor signals for the front location and the rear location (Figure 26) are shown to be the same. This does not imply that the corresponding electric fields have the same sign; that the fields are of opposite polarity is supported by our theoretical calculations. The reason that the polarity of the curves in Figure 28 is the same as the polarity of the

curves in Figure 26 results simply from experimental procedure. The cable connections were not altered when the cavity was rotated to change the location of the grid sensor from the "rear" location to the "front" location. When using the potential of the grid located farthest from the Hermes II anode as reference, the manner in which the rotation was accomplished caused a reversal in the observed signal. The sensor signal (see Figure 9) depicted in Figure 26 is V_{AB}; that in Figure 28 is V_{BA}.

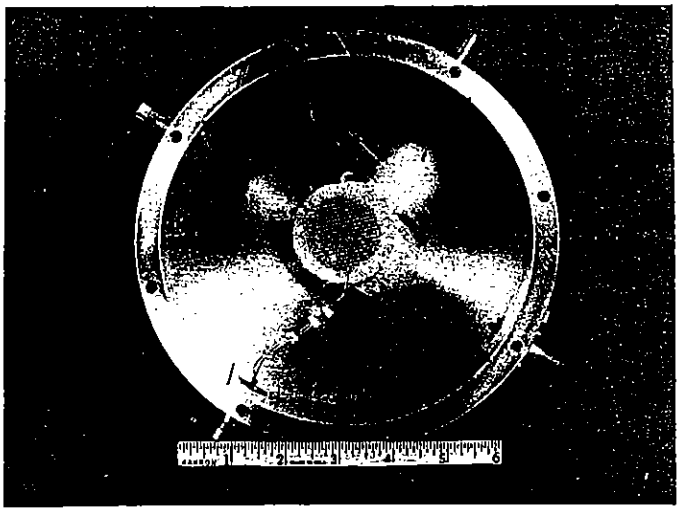

Figure 24. Photograph of the Dipole Grid Sensor Mounted Within the Cavity

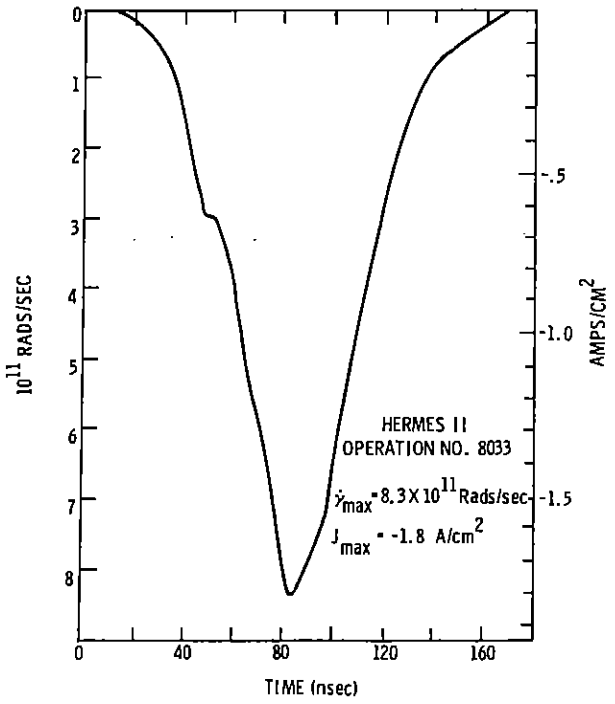

Figure 25. Compton Diode Signal for Hermes II Operation No. 8033

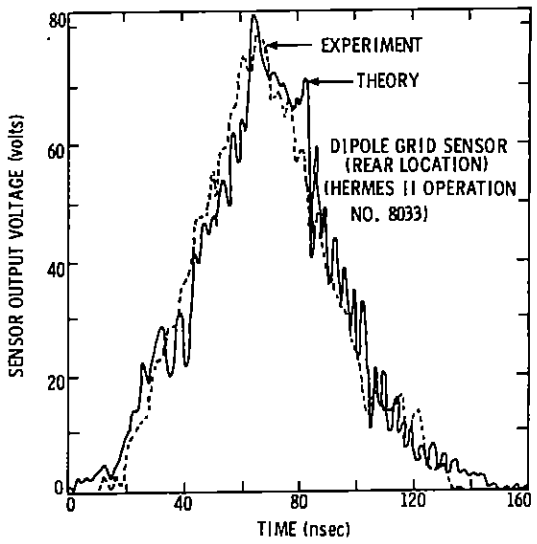

Figure 26. Comparison of Experimental Observation and Theoretical Prediction for the Dipole Grid Sensor Located Toward the Rear of the Cavity

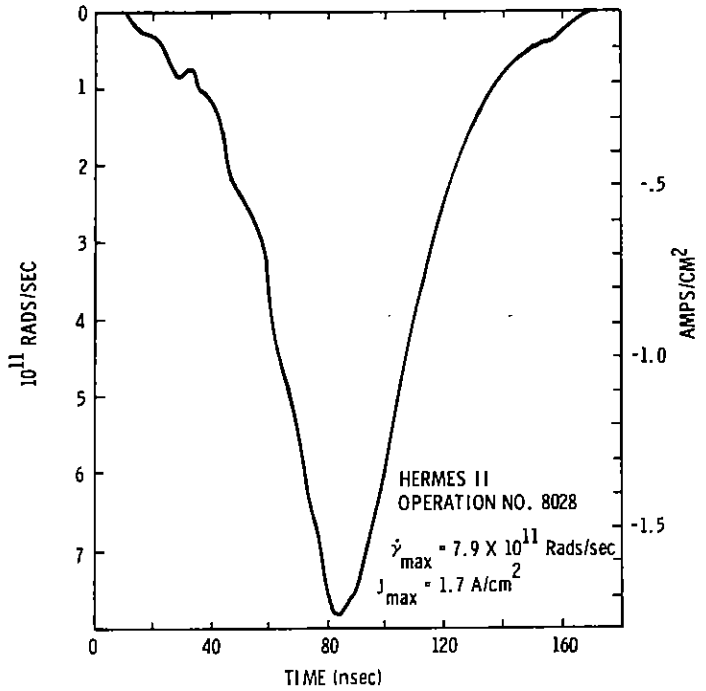

Figure 27. Compton Diode Signal for Hermes II Operation No. 8028

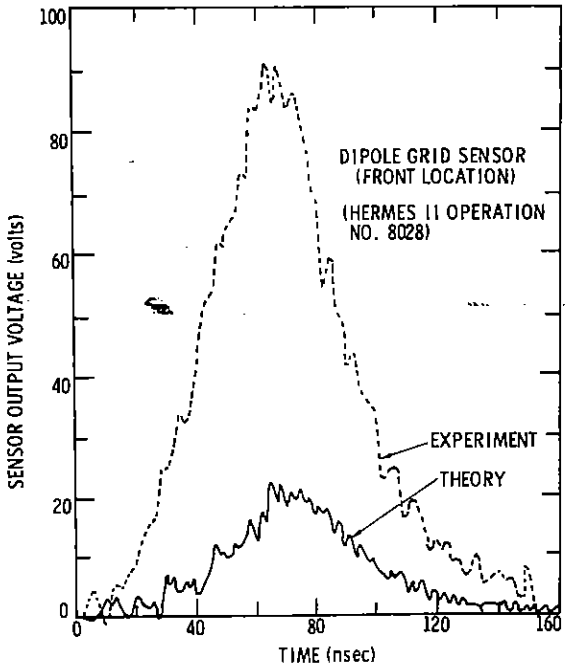

Figure 28. Comparison of Experimental Observation and Theoretical Prediction for the Dipole Grid Sensor Located Toward the Front of the Cavity

Discussion

Comparisons have been made between experimentally observed signals and theoretically predicted responses of various loop sensors and of a dipole grid sensor mounted in a cylindrical cavity exposed end-on in the Hermes II radiation environment. The theoretical predictions involved not only the determination of the electric and magnetic fields within the cavity, but also the coupling of these fields into the equivalent circuits of the sensors. No attempt has been made to explicitly equate the sensor signals with the values of the theoretically determined electric or magnetic fields.

Loop Sensor Response

The loop sensor signal is related to the area integration of the time rate of change of the azimuthal magnetic field threading the loop. Theoretical calculations indicate that the basic time behavior of the magnetic field follows closely that of the Compton current density. The time rate of change of the magnetic field, however, contains high-frequency components associated with the resonant frequencies of the cavity. In Figure 29, the theoretical temporal behavior of a specific $\dot{B}_\theta$ is shown. (The plot accuracy is one datum point per 0.5 nsec.) The frequency content in an associated loop sensor signal is limited by the inductance of the loop and the frequency response of the oscilloscope used for signal recording. The experimental results show that this dependence and the correlation between theory and experiment within the limits that can be ascribed to the accuracy, is good. Experimentally, the accuracy is limited by noise and oscilloscope response. Theoretically, the accuracy is limited by several factors. The model did not account for common-mode signals, within the loops, which result from more electrons being ejected from the sheath of the coaxial cable than from the center conductor. Baum[10] has pointed out that the design of the moebius loop should minimize this common-mode signal. We also believe that our theoretical predictions were limited by the degree of accuracy in digitizing the temporal behavior of the Compton current density pulse, as well as by the assumption that the spatial dependence of the current density did not vary with different Hermes II operations. In using the NUCYL computer code to predict the electromagnetic response of the cavity, it was assumed that the medium of the cavity possessed constant conductivity. We feel that this is one area of the theoretical modeling which can be improved. At the present time we are limited, however, as sufficient data do not exist to characterize adequately the temporal behavior of the photoconductivity. Previous theoretical investigations[4,7] have indicated that conductivity values comparable to the one used in the theoretical predictions of this study should not significantly affect the magnetic field response.

The temporal signature of the loop sensor response is highly dependent upon the time behavior of the radiation-produced current density pulse, because the loop sensor signal is an indirect measure of $\dot{B}_\theta$ or, equivalently, $\ddot{\gamma}$, and the current density is proportional to $\dot{\gamma}$. Therefore, the theoretical predictions are only as good as the assumption that the temporal behavior of the current density pulse is proportional to that of $\dot{\gamma}$.

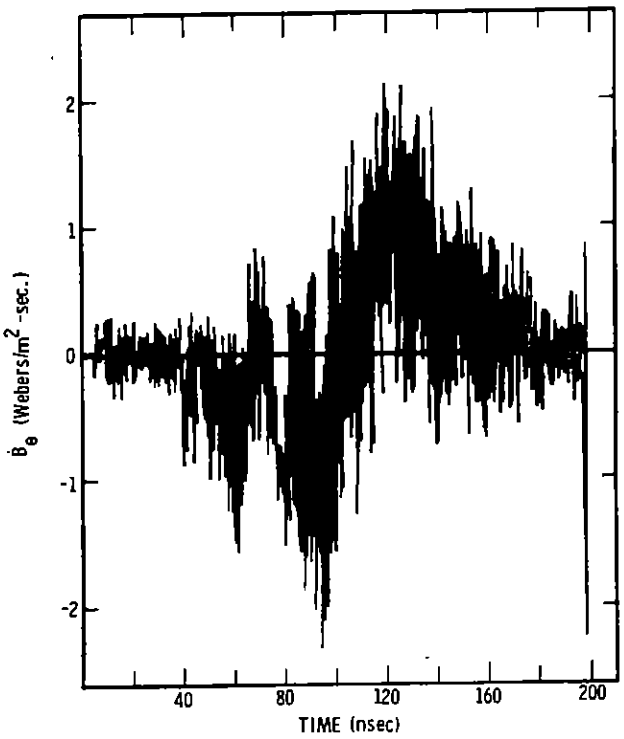

Figure 29. Temporal Behavior of the Time Rate of Change of the Magnetic Field at the Center of the Moebius Loop Sensor.

Dipole Grid Sensor Response

The theoretical model we proposed for the dipole grid sensor has been discussed in the Theory section. Again, the relationship between the dipole grid sensor signals and the actual electric field is only implicit. In Figure 30, we present the theoretical prediction of the electric field at the on-axis center of the grid sensor for the rear location case (Figure 26). The oscillatory behavior of the experimentally observed and theoretically predicted grid sensor signals shown in Figure 26 is attributed primarily to the electrical response associated with the grid sensor being capacitively and resistively coupled, through the geometry and the dielectric medium electrical properties, to the cavity wall. This coupling, in the theoretical equivalent circuit (Figure 9), is provided by the various R and C elements. The potential functions $\phi_1(t)$ and $\phi_2(t)$ associated with the equivalent circuit are rather smooth functions of time, not unlike the electric field depicted in Figure 29.

The one prediction which we feel is in serious disagreement with experiment is that associated with the dipole grid sensor located in the front of the cavity (Figure 28). The fact that we are able to predict the dipole grid sensor response when the sensor is located in the rear of the cavity lends credence to the theoretical model we developed. Two known phenomena, not accounted for in the theory, could have a greater effect on the dipole grid sensor response when the sensor is located in the front, as opposed to the rear, of the cavity. One phenomenon, termed the interface effect,[15] results from the differences in the forward-scattered and backward-scattered photon-produced electron currents within two different adjacent media. (For the

specific case considered here, the aluminum end plate is one of the media and the polyethylene spacer is the other.) To examine this effect, the results of Dellin and MacCallum[15] were used to calculate the spatial variation of the distributed electron current at the interface region. The calculations were made with the assumption that various monoenergetic photon beams were incident on the face of the cavity. The results indicate that the spatial variation of the distributed electron current density, which was used for the theoretical predictions, did not account for a small positive space charge in the polyethylene within an electron range from the aluminum end plate. The other physical phenomenon results from the fact that more electrons could have been ejected from one plate of the dipole grid sensor than from the other. Both of these phenomena are dependent upon the energy of the incident photons, and the effect caused by these phenomena should be greater at lower photon energies. It is not difficult to conclude, therefore, that these occurrences could preferentially affect the response of the dipole grid sensor when the sensor was located in the front of the cavity.

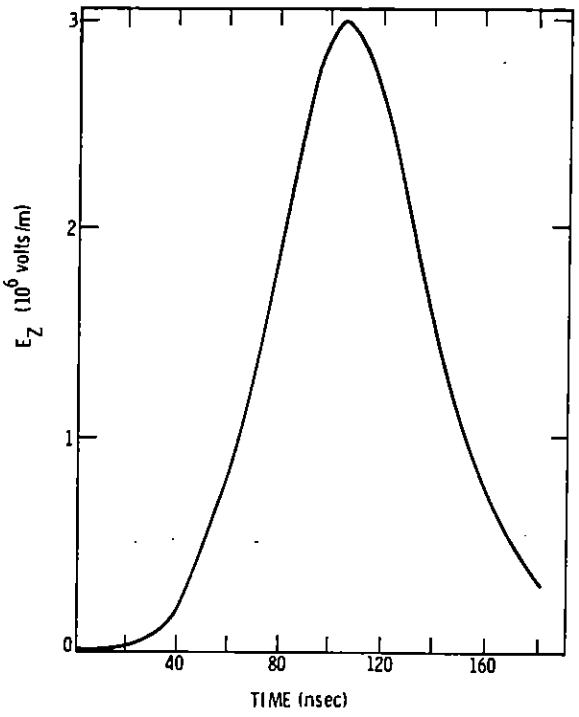

Figure 30. Temporal Behavior of the Axial Electric Field at the On-Axis Center of the Dipole Grid Sensor for the Rear-Location Case

The accuracy limitations of the theoretical model, applied to the dipole grid sensor response predictions, also include those mentioned in the discussion on the loop sensor responses. The effect of conductivity on the electric-field-related predictions, however, should be significant. This can be readily perceived by noting that if the medium conductivity is assumed to be zero (a hypothetical limiting case), the magnitude of the electric fields will continue to increase, reaching a nondecaying maximum when the spatially divergent current density pulse terminates.

Conclusions

The goal of the study, to verify by experimentation the theoretical predictions of the electromagnetic response of a cavity, was satisfactorily fulfilled. The verification was implicit, since experimentally observed sensor responses were compared to theoretically predicted sensor responses. We feel that our theoretical modeling is adequate and that the extent to which this type of study could continue depends upon the refinements one would like to make to such a model.

References

1. W. D. Brown, IEEE Trans. Nucl. Sci. NS-19 68 (1972)

2. W. R. Faust, J. Appl. Phys. 43 3983 (1972)

3. D. L. Mangan and G. J. Scrivner, IEEE Trans. Nucl. Sci. NS-19 41 (1972)

4. D. L. Mangan and G. J. Scrivner, "Numerical Calculations of Radiation Driven Cavity Response." Presented at the DNA Sponsored IEMP Symposium, San Diego, Calif., Feb. 6-8, 1973. To be published in the Proceedings of the Symposium.

5. A. R. Wilson, "IEMP Behavior Prior to Breakdown." Presented at the DNA Sponsored IEMP Symposium, San Diego, Calif., Feb. 6-8, 1973.

6. D. E. Merewether and W. A. Radasky, "Nonlinear Electromagnetic Fields Within a Cylindrical Cavity Excited by Ionizing Radiation." Presented at the DNA Sponsored IEMP Symposium, San Diego, Calif., Feb. 6-8, 1973.

7. G. J. Scrivner and D. L. Mangan, IEEE Trans. Nucl. Sci. NS-20 108 (1973)

8. D. C. Osborn, "Axially Symmetric IEMP Studies With Hermes." Presented at the DNA Sponsored IEMP Symposium, San Diego, Calif., Feb. 6-8, 1973.

9. N. J. Kreidl and G. E. Blair, Nucleonics Vol. 14 56 (1956)

10. Private communication, R. L. Schuch, Sandia Laboratories, Albuquerque

11. C. E. Baum, "Characteristics of the Moebius Strip Loop." AFWL EMP 1-1, Note 7 (June 1970)

12. C. E. Baum, "Maximizing Frequency Response of a B Loop." AFWF EMP 1-1, Note 8 (1970)

13. R. E. Partridge, "'Invisible' Absolute E-Field Probe." AFWL EMP 1-1, Note 2 (June 1970)

14. C. E. Baum, "A Technique for Measuring Electric Fields Associated With Internal IEMP." AFWL EMP 1-1, Note 24 (June 1970)

15. C. J. MacCallum and T. A. Dellin, J. Appl. Phys., Vol. 44, No. 4, 1878 (1973)

16. Old Chinese proverb

17. W. H. Sullivan and R. L. Ewing, IEEE Trans. Nucl. Sci. NS-18 310 (1971)

18. R. C. Weingart, R. H. Barlett, R. S. Lee, and W. Hofer, IEEE Trans. Nucl. Sci. NS-19 15 (1972)